nature communications



Article

https://doi.org/10.1038/s41467-025-64256-7

Solution-processable and photo-curable system for low-cost and scalable transient electronics

Received: 13 May 2025

Accepted: 10 September 2025

Published online: 15 October 2025



Won Bae Han ^{1,2}, Sungkeun Han ¹, Taekyung Kim ^{3,4}, Tae-Min Jang ^{1,5}, Gwan-Jin Ko^{1,6}, Jaesoon Joo³, Taewoo Kim³, Kyu-Sung Lee^{4,7}, Young-Min Shon ^{4,8}, Eunkyoung Park⁹, Venkata Ramesh Naganaboina ¹⁰ & Suk-Won Hwang ^{1,11,12} ⊠

The discovery of non-toxic, bioresorbable silicon electronics is a major breakthrough in the fields of transient, dissolvable biomedical implants and environmental monitors, as it opens up the possibility of producing versatile components based on established semiconductor processes. However, given the limited lifespan of such electronics, it is essential to consider economical manufacturing and production strategies that reduce the unit price for commercialization. Here, we introduce a solution-processable and photopatternable approach that is facile, cost-effective, and widely accessible for a monolithic 3D fabrication of soft, stretchable, and transient electronics. Optimized chemical synthesis and rational materials engineering yield biodegradable/biocompatible organic insulators, semiconductors, and conductors that can be layered/assembled in sophisticated configurations without impairing underlying components. Direct solution-casting of the materials enables the fabrication of sensors with various modalities and transistors. In vivo implantation of soft, conformable electrode arrays into the brain and heart of animal models demonstrates spatiotemporal electrophysiological monitoring (electroencephalography and electrocardiography) and therapeutic interventions (epileptic seizure suppression and cardiac pacing), highlighting the broad applicability in diverse bio-integrated electronic systems.

Large-scale, high-performance transient electronics opens new avenues for innovative applications across multiple research fields, including temporary biomedical implants¹⁻⁹, sustainable/eco-conscious sensors^{10–14}, and defense and security systems^{15–17}, where non-

transient counterparts may not be practical or desirable. One of the key findings in transient technology is the water-soluble capability of silicon, which offers a wide range of silicon-based electronic components (e.g., complementary metal-oxide-semiconductor (CMOS),

¹KU-KIST Graduate School of Converging Science and Technology, Korea University, Seoul 02841, Republic of Korea. ²School of Electronic Engineering, Kyonggi University, Suwon, Gyeonggi-do 16227, Republic of Korea. ³Biomedical Engineering Research Center, Samsung Medical Center, Seoul, Republic of Korea. ⁴Department of Medical Device Management and Research, SAIHST, Sungkyunkwan University, Seoul, Republic of Korea. ⁵Semiconductor R&D Center, Samsung Electronics, Gyeonggi-Do, Republic of Korea. ⁶Display Research Center, Samsung Display, Gyeonggi-Do, Republic of Korea. ⁷Department of Urology, Samsung Medical Center, Sungkyunkwan University School of Medicine, Seoul, Republic of Korea. ⁸Department of Neurology, Samsung Medical Center, Sungkyunkwan University School of Medicine, Seoul, Republic of Korea. ⁹Department of Biomedical Engineering, Soonchunhyang University, Asan, Republic of Korea. ¹⁰Department of Electronics and Communication Engineering, Amrita School of Engineering, Amrita Vishwa Vidyapeetham, Amaravati Campus, Amaravati, Andhra Pradesh, India. ¹¹Center for Biomaterials, Biomedical Research Institute, Korea Institute of Science and Technology (KIST), Seoul, Republic of Korea. ¹²Department of Integrative Energy Engineering, Korea University, Seoul, Republic of Korea. ²E-mail: dupong76@korea.ac.kr

diodes, ring oscillators, logic circuits, radio frequency (RF) components) were able to be fabricated using established microelectronic processes, although additional processes were required to create a complete product, particularly for mechanically flexible forms^{18,19}. However, given the inherent and key nature of transient electronic components -- degraded or disposed after a temporary lifespan -- such energy-intensive and complex manufacturing processes raise critical concerns about sustainability and economic feasibility, potentially undermining market competitiveness and commercial viability. In this context, cost-efficient, easy-to-implement strategies might not only improve the scalability and practicality of transient systems but also align with the core principles of minimizing waste and maximizing efficiency. Previous approaches involving screen^{20,21}, inkiet^{22,23}, and three-dimensional (3D) printing^{24,25}, have been explored based on various organic and/or inorganic electronic materials and composites; however, they typically suffered from resolution, consistency, and device durability. In a similar manner, the advanced laser scanning ablation process offers excellent precision and resolution of inorganic or organic thin films²⁶⁻²⁸, while it also has several drawbacks, such as material restrictions, high equipment costs, and restricted scalability.

In the following, we introduce a set of solution-processable and photo-patternable electronic materials tailored as substrates/insulators, semiconductors, and conductors for straightforward, cost-effective, and scalable fabrication of soft, stretchable, transient electronics. Chemical synthesis and materials engineering optimize the properties of these electronic materials to be compatible with the solution process while retaining outstanding electrical and mechanical properties, and sequential, layer-by-layer deposition allows for diverse, deformable electronic components with resolutions down to a few microns. In vivo animal tests demonstrate the diagnostic and therapeutic capabilities of the transient system in the central organs such as the brain and heart, highlighting the potential of solution-based transient electronics across various research fields.

Results

Monolithic 3D fabrication of soft, transient elastomeric electronics

Figure 1a illustrates a facile and cost-effective strategy for monolithic 3D fabrication of soft, stretchable, and transient electronics through multiple implementations of solution casting and direct photopatterning of organic insulating, semiconducting, and conducting materials. These key electronic components were developed through a combination of chemical and physical methods to achieve solutionprocessable, photo-curable, deformable, biocompatible, and/or degradable properties. For the substrate/insulator material, a biodegradable elastic polyol, i.e., poly(l-lactide-co- ε -caprolactone) (PLCL) diol, was chemically conjugated with acrylic acids via urea bonds (referred to as UV-PLCL, Supplementary Fig. S1), which could undergo crosslinking in the presence of 2,4,6-trimethylbenzoyldiphenylphosphine oxide (TPO, photoinitiator) and trimethylolpropane tris(3-mercaptopropionate) (TTMP, crosslinking enhancer). The semiconductor material comprised a PLCL polymer matrix with poly(3-hexylthiophene) (P3HT) as a semiconducting element, Zonyl FS-300 as a surfactant, and a double-end functionalized diazirine crosslinker. The conductor material included poly(3,4-ethylenedioxythiophene) polystyrene sulfonate (PEDOT:PSS), 2,4-hexadiyne-1,6-diol (HDD), and Zonyl FS-300, serving as an electrically conducting substance, crosslinker, and surfactant, respectively. Appropriate stoichiometry control, choice of solvents, and tailored curing/ developing conditions enabled the formation of multiple layers for sophisticated device structures with a few micron resolution, without impairing the physical and electrical properties of the underlying layers. As a proof-of-concept, we fabricated a 4-inch multifunctional integrated electronics array (Fig. 1b) with an ultrathin dimension (a total thickness of ~3 µm), consisting of thin film transistors (TFTs), a microheater, a capacitor, pressure sensors, and an inductive coil. The proposed strategy was able to complete such large-scale electronic device within a short period of time and low cost, offering significant advantages over traditional, tedious, and pricey manufacturing methods (Supplementary Table S1). Since the overall system has an ultrathin geometry with intrinsically elastic yet tough characteristics, the device was able to withstand various deformation modes such as stretching, twisting, and poking (Fig. 1c and Supplementary Fig. S2), and to facilitate seamless integration with the irregular surfaces of a brain phantom, which is particularly beneficial for reliable interfaces with biological tissues and organs in biomedical and healthcare applications²⁹⁻³¹ (Fig. 1d). Figure 1e demonstrates the physical transience of a representative device, when immersed in an accelerated condition (phosphate-buffered saline, PBS, pH 13, 37 °C). Over time, the device gradually lost its structure primarily due to dissolution of PLCL via hydrolysis-induced ester linkage cleavage^{32,33}, leading to disintegration of the conductor layer into small fragments after 21 days of immersion.

Solution-processable and photo-patternable electronic materials

UV-curable polymers served as a fundamental building block for stretchable, biodegradable substrate and insulating layers (Fig. 2a). Under exposure to 365 nm-wavelength light, the photoinitiator, i.e., TPO, generated a free radical to initiate the crosslinking of unsaturated carbon-carbon double bond (C=C) at both ends of UV-PLCL monomers, forming a densely entangled network (Supplementary Fig. S3). Here, the inclusion of thiol additive, i.e., TTMP, facilitated radical transfer and thus efficient polymerization against oxygen at ambient conditions, contributing to stable film production³⁴. Figure 2b displays the mechanical properties of resultant films (100 μmthick) depending on different molecular weights (M_n) of UV-PLCL monomers. As M_n increased, the films became softer and more elastic, while the toughness across all M_n fell into 10-20 MJ/m³ (Supplementary Fig. S4), comparable to those of well-known elastomers such as polydimethylsiloxane (PDMS)³⁵ and styrene-ethylenebutylene-styrene (SEBS)³⁶. All films exhibited a similar dielectric constant of ~3.5 at 1 kHz with a slight decrease at higher frequencies (Fig. 2c), and additional physical properties, including optical transparency and thermal stability, appear in Supplementary Fig. S5. Degradability is another critical factor for transient electronics. In this regard, Fig. 2d presents the dissolution behavior of the substrate/insulator films. The results indicated that the higher M_n led to faster degradation primarily due to the abundance of ester bonds, and these dissolution rates varied with temperature and pH levels (Supplementary Fig. S6), which is consistent with previous studies37,38.

For the semiconductor layer, P3HT nanofibrils (NFs) were synthe sized through the self-assembly of P3HT chains via π - π stacking (Supplementary Fig. S7) due to the superior crystallinity and carrier mobility over neat P3HT³⁹. Photoirradiation with a 365 nm wavelength initiated carbene formation on end groups of a diazirine crosslinker, which was then inserted into unconjugated C-H bonds of both P3HT and PLCL, forming a stretchable and decomposable semiconducting network (Fig. 2e). Synthesis of the diazirine crosslinker and the detailed crosslinking mechanism appear in Supplementary Fig. S8. A crosslinker ratio of ~2 yielded a fully crosslinked, robust film (Fig. 2f). Deviations from this threshold, however, led to decreased tolerance to organic solvents or lower conductivity. The ratio of PLCL to P3HT provides a tunable factor for conductivity and stretchability of the semiconducting layer (Fig. 2g). The optimum ratio (PLCL:P3HT, 8:2) was selected based on electrical/mechanical characteristics (thicknessand strain-dependent electrical properties appear in Supplementary Fig. S9). This semiconducting film was dissolved in PBS (pH 7) at 37 °C

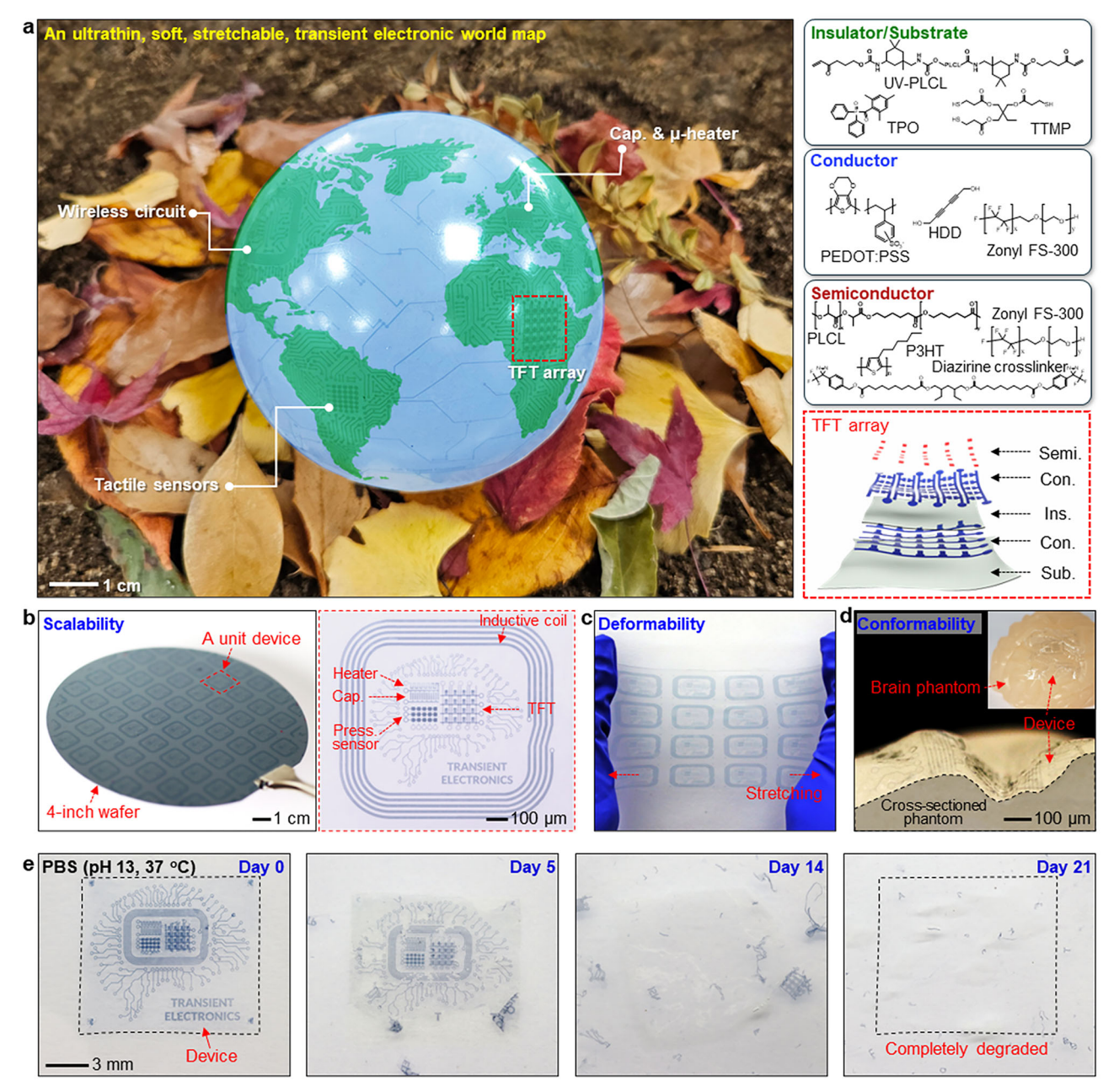


Fig. 1 | **Facile and cost-effective fabrication of soft, stretchable, transient electronics at wafer-scale. a** Photograph of an ultrathin, soft, and stretchable transient electronic world map conformally wrapped on a globe, which was fabricated through multiple depositions of solution-processable, photo-patternable electronic materials including insulators, conductors and semiconductors (left), chemical structures of constituting components for the electronics materials (top right), and schematic illustration of a thin-film transistor (TFT) array (bottom right). The electronic world map was colorized for ease of viewing. UV-PLCL, ultraviolet (UV)-curable and biodegradable elastomer, poly(l-lactide-co-ε-caprolactone); TPO, 2,4,6-trimethylolpropane tris(3-

mercaptopropionate); PEDOT:PSS, poly(3,4-ethylenedioxythiophene) polystyrene sulfonate; HDD, 2,4-hexadiyne-1,6-diol; P3HT, poly(3-hexylthiophene). **b** Optical images of a wafer-scale, ultrathin elastomeric transient electronics array (left) and a magnified view of a unit device featuring a microheater, capacitor, pressure sensor array, TFT array, and inductive coil (right). (**c**,**d**) Photographs of the transient electronics under mechanical strain (**c**) and in conformal contact with the wrinkled surface of a brain phantom (**d**). **e** Time-sequential images showing the gradual dissolution of the transient elastomeric electronics under accelerated conditions (phosphate-buffered saline, PBS, pH 13) at body temperature (37 °C).

with a slower degradation rate (0.12 μ m/day) than that of a pristine PLCL film (0.21 μ m/day), which could be attributed to the hydrophobic nature of P3HT NFs (Fig. 2h).

Figure 2i describes the topochemical polymerization process for the conducting layer. When exposed to 254 nm UV light, diacetylenes of HDD were crosslinked into polydiacetylene, with its hydroxyl groups electrostatically interacting with PEDOT domains, as detailed in Supplementary Fig. S10. This reaction not only transformed the PEDOT structure into linear and extended coil conformation for

enhanced conductivity, but also provided water resistance, allowing exposed patterns to remain intact after developing with deionized water⁴⁰. As depicted in Fig. 2j, the optimum HDD concentration of -10 % was necessary for effective patterning since higher concentrations led to spontaneous crosslinking of diacetylenes even without photoirradiation, and to a brittle network. Lower concentration, on the other hand, failed to achieve sufficient crosslinking density, resulting in removal of the desired pattern during development. To further enhance the electrical properties of

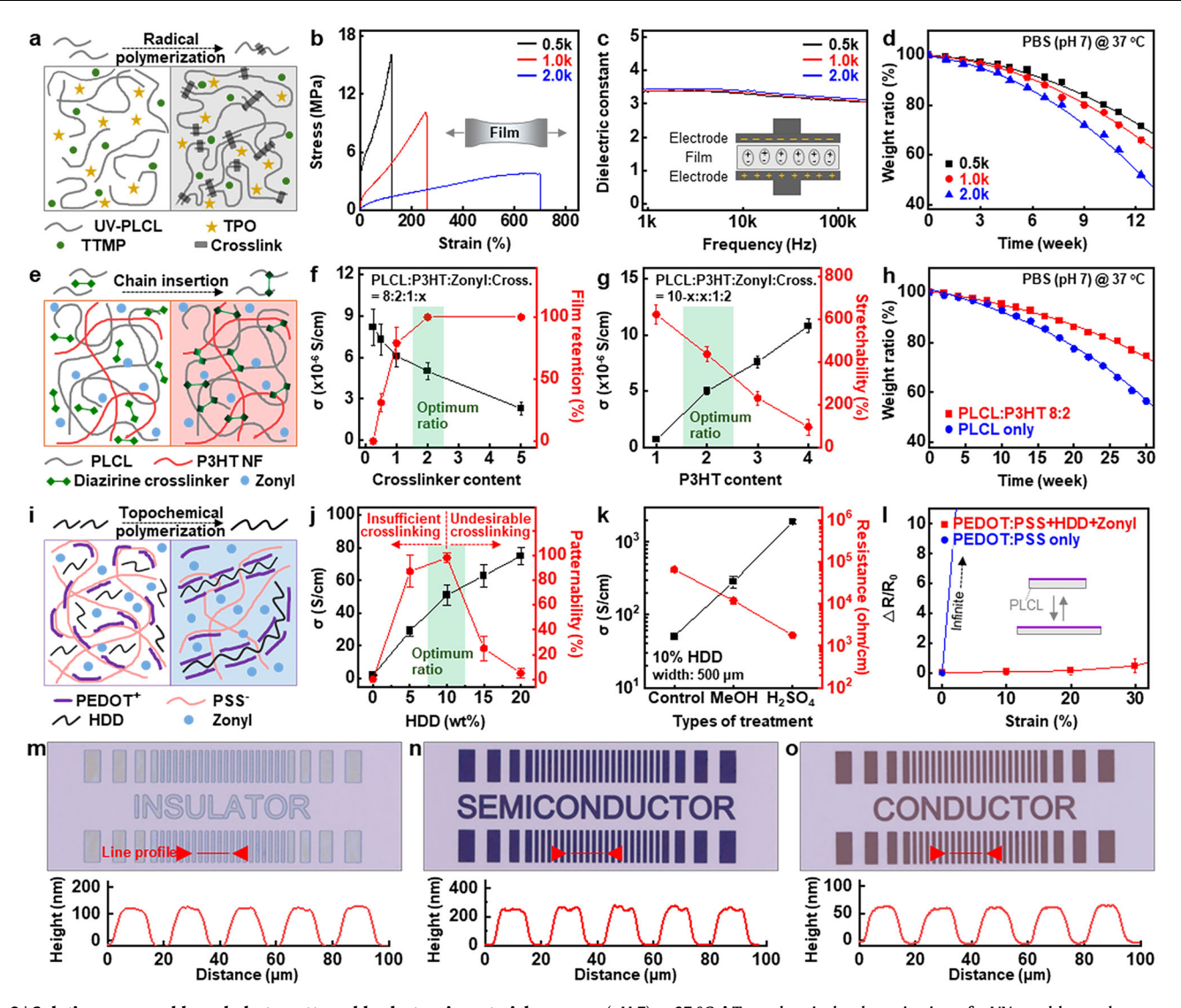


Fig. 2 | **Solution-processable and photo-patternable electronic materials. a** Radical polymerization of UV-PLCL in the presence of TPO as a photoinitiator and TTMP as a crosslinking enhancer. Characterization of polymerized UV-PLCL (insulator) films synthesized from different molecular weights of PLCL prepolymer: stress-strain curves (**b**), dielectric constants (**c**), and dissolution profiles in PBS (pH 7) at 37 °C (**d**). **e** Photo-responsive carbene insertion-based crosslinking of a semiconductor composed of PLCL as a polymer matrix, P3HT nanofibers (NFs) as a semiconducting element, Zonyl FS-300 as a surfactant, and a double-branched diazirine crosslinker. **f** Correlation between electrical conductivity and pattern yield of the semiconductor film as a function of crosslinker content. Data are presented as mean values \pm standard deviation. n = 5 independent samples. **g** Conductivity and stretchability of semiconductors with different P3HT fractions. Data are presented as mean values \pm standard deviation. n = 5 independent samples. **h** Dissolution behaviors of semiconductor films with and without P3HT in PBS

(pH 7) at 37 °C. **i** Topochemical polymerization of a UV-curable conductor consisting of PEDOT:PSS as a conducting substance, HDD as a crosslinker, and Zonyl FS-300 as a surfactant. **j** Electrical conductivity and pattern yield of conductors with varying HDD contents. Data are presented as mean values \pm standard deviation. n=5 independent samples. **k** Changes in electrical properties of conductor films with 10 wt% of HDD after treatments with methanol (MeOH) and sulfuric acid (H₂SO₄) for 2 min. Data are presented as mean values \pm standard deviation. n=5 independent samples. **l** Comparison of strain-dependent electrical performance between pristine PEDOT:PSS and the optimized conductor (10 wt% HDD). Data are presented as mean values \pm standard deviation. n=5 independent samples. Optical images (top) and corresponding morphology profiles (bottom) of patterned insulator (**m**), conductor (**n**), and semiconductor (**o**) films with minimum line widths of several micrometers.

patterned traces, secondary doping was implemented by immersing the samples in methanol or 40 % $\rm H_2SO_4$ for 3 min, followed by rinsing with deionized water (Fig. 2k). This treatment altered PEDOT structure from benzoid to quinoid configurations, significantly increasing conductivity to ~2000 S/cm and reducing resistance to ~1000 ohm/cm without physical degradation (Supplementary Fig. S11). Figure 2l demonstrates the electrical stability of the conductor layer under mechanical strains. The resistance remained nearly unchanged up to 30 % strain, in contrast to the significant increase observed in a pristine PEDOT:PSS film. Such enhanced strain tolerance was attributed to crack suppression by the crosslinked

network and added surfactant, i.e., Zonyl FS-300 (Supplementary Fig. S12), and the mechanical stability was further validated through cyclic bending tests (Supplementary Fig. S13).

Finally, the patterning resolution and layer uniformity of the insulator, semiconductor, and conductor were demonstrated through microscopic imaging and profilometry. As shown in Fig. 2m-o, each layer exhibited nanoscale thicknesses (50 nm to 300 nm) and a minimum line width of several microns with high precision. The thickness could be controlled by varying the spinning rate and employing multiple patterning processes (Supplementary Fig. S14).

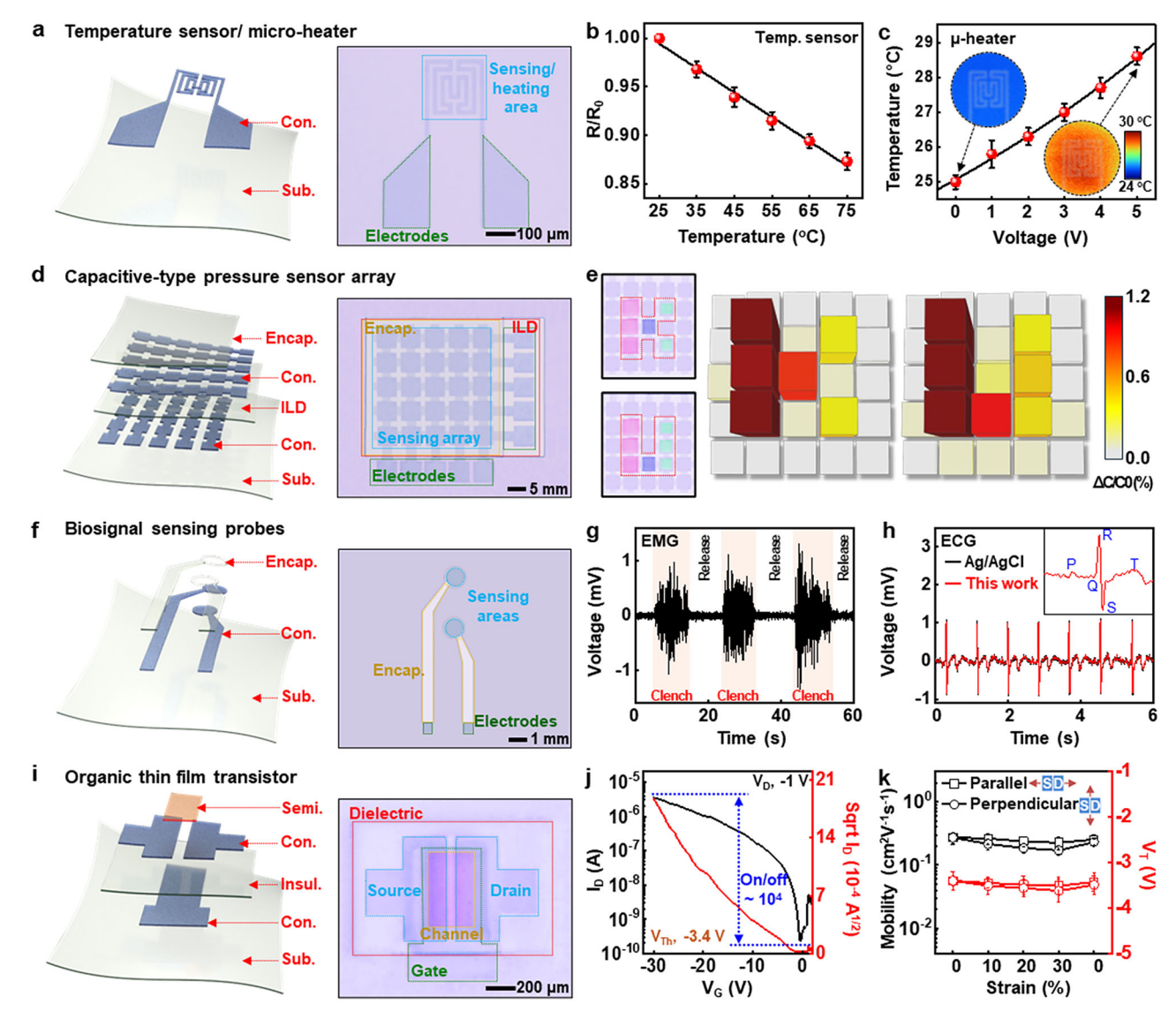


Fig. 3 | **Diverse functional electronic components.** a Exploded (left) and optical views (right) of an elastomeric resistive temperature sensor/heater. **b** Fractional change in resistance of the temperature meter as a function of temperature. **c** Joule heating-induced temperature gradients of the resistive heater depending on a range of applied voltages. **d** Exploded view diagram (left) and optical image (right) of a 5 \times 5 array of capacitive-type pressure sensors. **e** Pressure distributions measured by placing small blocks (-1.0, -0.6, and -0.3 g for red, blue, and green, respectively) with 'K' and 'U' letters on the sensor array. **f** Description of individual layers (left) and optical image (right) of a 2-channel electrophysiology (EP) sensor/

electrical stimulator. **g** Continuous, real-time measurements of electromyography (EMG) signals for different hand motions, 'clench' and 'release'. **h** Comparison of electrocardiography (ECG) signals acquired with commercial Ag/AgCl electrodes and the EP sensor. **i** Exploded view drawing (left) and optical image (right) of a p-channel field effect transistor (TFT; channel length (L) and width (W) are $50 \, \mu m$ and $500 \, \mu m$, respectively). **j** Transfer characteristics of the transistor, with on/off ratio > -10^4 . **k** Variation in charge carrier mobility and threshold voltage (V_T) of the transistor under cyclic loading of horizontal and vertical strains up to $30 \, \%$. Data are presented as mean values \pm standard deviation. n = 5 independent samples.

Demonstrations of soft, transient electronic components

Multiple deposition and patterning of the developed electronic materials facilitate the integration of diverse functional components tailored for applications in soft, transient elastomeric electronics, such as wearable sensors, implantable devices, and biodegradable circuits. One example includes a microscale, resistive component for a temperature meter and heater in a fractal configuration (Fig. 3a). The relative resistance of the PEDOT:PSS-based conductive pattern linearly decreased with increasing temperature with a temperature coefficient of resistance of -0.254%/°C (Fig. 3b), comparable to previously reported transient temperature sensors^{41–43}. Applied voltages produced heat via Joule heating, following the relation $Q = V^2/R$, where Q, V, and R represent the generated heat, applied voltage, and resistance of the conductor, respectively (Fig. 3c). The heating rate could be modulated by adjusting the resistance of the conductor

layer (Supplementary Fig. S15). Integrating the conductor with a semiconducting layer yielded a stretchable strain sensor, which exhibited consistent responses under applied mechanical deformation (Supplementary Fig. S16). Furthermore, pressure sensing capability was demonstrated using a capacitive-type pressure sensor array (5×5) consisting of top and bottom electrodes with an interlayer dielectric in a sandwich structure (Fig. 3d). External pressures caused a decrease in the distance between the conductive layers, leading to a change in capacitance, which recognized the letters 'K' and 'U' through small blocks with different weights (Fig. 3e). Such capacitance change was sufficiently high even under low pressures, with a sensitivity of ~0.020/kPa in the range of 0–1000 Pa (Supplementary Fig. S17), which falls within the range reported for transient pressure sensors^{2,44,45}. The material platform also supported bioelectrical sensing applications. A soft, transient probe was developed

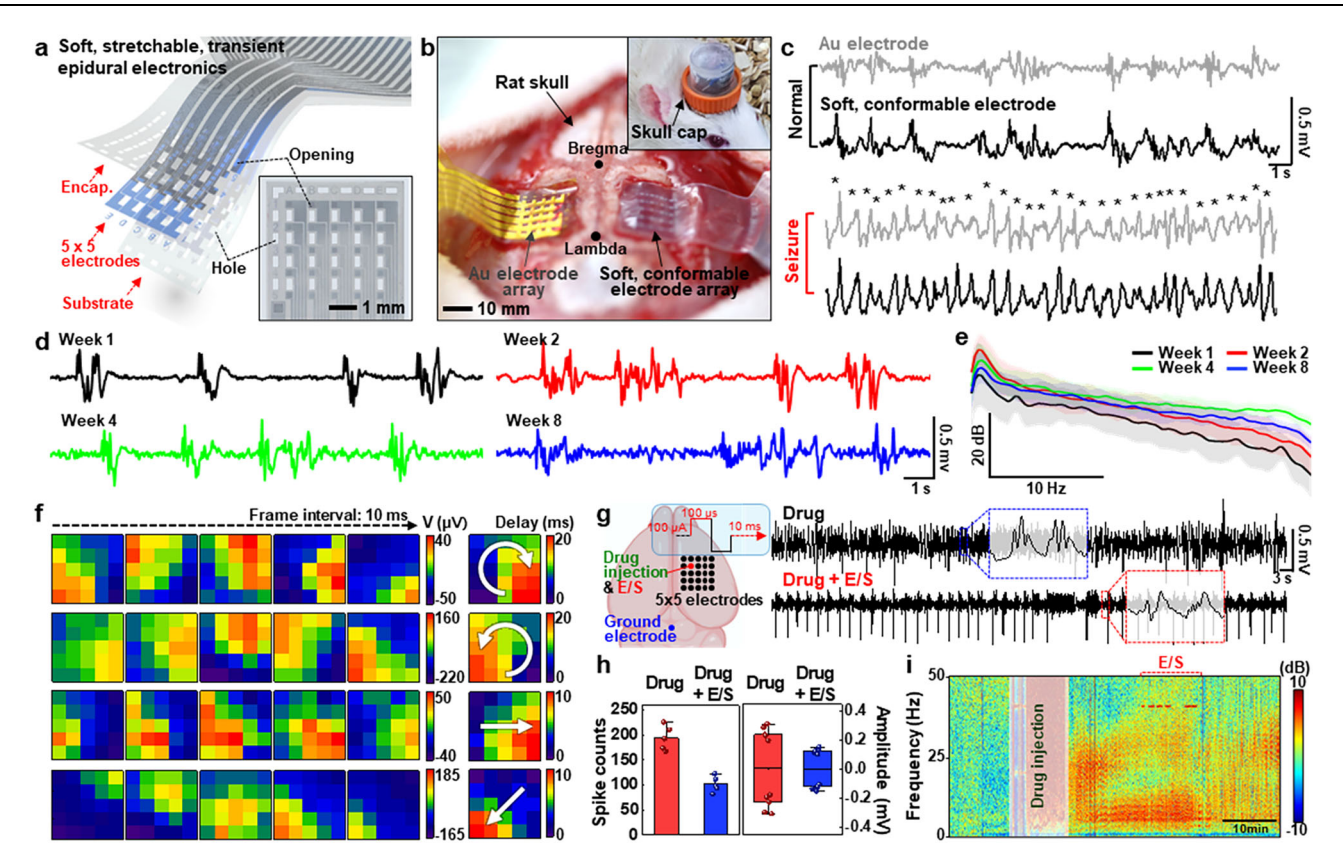


Fig. 4 | **Soft, conformable, and transient electrode arrays for neural and cardiac diagnosis and therapy. a** Schematic illustration of a 5×5 transient epidural electrode array capable of electrocorticography (ECoG) monitoring and electrical neurostimulation, and an optical image of the active region of a representative device in the inset. **b** Photographs of gold (Au)-based (left hemisphere) and soft, conformable transient (right hemisphere) neural electrode arrays implanted onto cortical surfaces in left and right hemispheres of a rat, respectively, with the inset showing a custom-designed skull cap for stable, long-term implantation. **c** Comparative analysis of recorded ECoG signals from the Au and transient neural electrodes during normal and acute seizure activities. **d** Long-term, stable ECoG measurements with soft, transient neural electrodes implanted in rat models over

several weeks. **e** Power spectral density (PSD) analyses of the recorded signals. Data are presented as mean values \pm standard deviation. n=3 biologically independent animals per group. **f** Spatiotemporal mapping of ECoG biopotential patterns, revealing distinct spiking flows during a seizure. **g** Schematic of the experimental setup for neural recording and stimulation (left), and ECoG traces recorded during a seizure before and after electrical stimulation (E/S) (right). **h** Comparison of the average count/amplitude of spiking events before and after electrical stimulation. Data are presented as mean values \pm standard deviation. n=5 biologically independent animals per group. **i** Time-frequency analysis of ECoG signals before and after drug injection and electrical stimulation.

for electrophysiology recordings, capable of capturing both electromyography (EMG) and electrocardiography (ECG) signals (Fig. 3f). The signals demonstrated the ability to perceive hand motions and monitor cardiac rhythms with clear QRS complexes and P/T peaks, comparable to those of commercial silver (Ag)/silver chloride (AgCl) electrodes (Fig. 3g, h) These sensing performances retained nearly unchanged even under mechanical strains ranging from 0 % to 30 % (Supplementary Fig. S18). The detailed measurement setup is described in the Methods section. The proposed strategy is also useful to construct soft, transient TFTs for active-matrix array-based multiplexed and high-performance devices. As shown in Fig. 3i, a bottom-gate TFT was constructed with a channel length/width of 50/500μm. Measured transfer curves (V_D, -1 V) in Fig. 3j exhibited mobility of 2.73 cm²/(V·s), an on/off ratio of ~10⁴, and a threshold voltage (V_T) of -3.4 V, comparable with those shown in recently reported soft, non-transient transistors⁴⁶⁻⁴⁹. I-V characteristics for different channel lengths appear in Supplementary Fig. S19. This transient transistor could be stretched without malfunction (Fig. 3k). Under strains up to 30% parallel and perpendicular to the devices, the mobility and V_T slightly changed; however, these values were almost restored after the removal of strains. Replacing inelastic P3HT with fully stretchable, degradable semiconducting materials can be implemented to further enhance the tolerance to strain for practical uses. A comprehensive comparison of our devices with previously

reported transient electronics in terms of materials, performance, fabrication processes, and applications is presented in Supplementary Table S2.

Soft, stretchable, transient electronics for biomedical applications

Evaluation of the proven system through living organisms can provide the potential for envisioned research areas. As a core example, a soft and stretchable 5 × 5 neural electrode array was fabricated to conduct in vivo spatiotemporal neurophysiologic monitoring and on-demand electrotherapy of neurological disorders (Fig. 4a). Detailed device information, electrochemical impedance and charge storage/injection capacity (CSC/CIC), and long-term stability appear in Supplementary Figs. S20, S21, and S22, respectively. It is noteworthy that the lithography-assisted fabrication method can allow for scalability to different device sizes and channel counts for various applications. Figure 4b shows an image of the transient device and a conventional polyimide/gold/polyimide (PI/Au/PI) neural probe as a control, both implanted onto the craniotomy-exposed cortex (-5 x - 5 mm²) of an anaesthetized rat. Here, the soft and stretchable form factor improved conformal contacts to the brain surface, enabling to form chronically stable interfaces with cortical tissues⁵⁰⁻⁵². For long-term stable operation in awake animal models, devices were connected to a pin connector and encased in a custom-made head stage (details in

Supplementary Fig. S23). Electrocorticography (ECoG) potentials recorded from both devices exhibited distinct features under normal and epileptic conditions (Fig. 4c). Specifically, the signals exhibited large-scale oscillatory behaviors at various times and locations in the normal state (top) and high-amplitude epileptic spikes and discharges after acute induction of seizure with penicillin (bottom), a quantitative analysis of the signal-to-noise ratio demonstrated that there was no statistical discrepancy between the two devices (Supplementary Fig. S24). The high-fidelity performance was maintained without noticeable deterioration for 8 weeks of implantation (Fig. 4d, e) (neural response to toe pinch appears in Supplementary Fig. S25). Spatiotemporal mapping of ECoG signals recorded with the 25 channels in Fig. 4f revealed specific patterns of neural wave propagation (e.g., clock spiral, clockwise spiral, left-to-right sweep, and upper-right to lower-left diagonal), providing not only clear evidence of seizures but also an epileptogenic zone for clinical intervention. To explore the electrotherapeutic function for epilepsy symptoms, an electrical pulse (amplitude, 100 µA; pulse width, 100 µs; frequency, 130 Hz) was applied at the injection site of penicillin for a total duration of 10 min using a unipolar configuration against a stainless-steel counter-electrode in the cerebellum (Fig. 4g). Post-stimulation ECoG signals showed substantial suppression of epileptic spikes and discharges compared to pre-therapy recordings (additional data in Supplementary Fig. S26). Quantitative analysis confirmed reductions in spike count and amplitude by approximately 47 % and 51 %, respectively (Fig. 4h). The efficacy was more evident in the time-frequency analysis (Fig. 4i and Supplementary Fig. S27). Compared to signal strengths before drug injection (penicillin), an increase in power was apparent across all bands after the injection, particularly in the theta (4-8 Hz) and beta (13-30 Hz) ranges. However, electrical stimulation resulted in an overall decrease of signal activity across the entire bandwidth, indicating the ability to suppress seizures. Ultrathin geometry and mechanical resilience of the proposed electronic system also enable seamless operation on elastic, time-dynamic organs, e.g., heart, Corresponding demonstrations or cardiac monitoring and pacemaking are provided in Supplementary Fig. S28.

To confirm the biocompatibility of materials and devices for long-term implantation, we implanted transient neural electrodes into the rat brains and examined biological responses at several stages of post-implantation through immunohistochemistry. Although there were slight increases of CD68 and TNF- α in the tissues of rats implanted with electrodes for a period of 10 weeks, no significant tissue damage and inflammatory infiltration into the brain tissue were detected (Supplementary Fig. S29). The results of blood and weight tests were within normal ranges, confirming the long-term safety of the system (Supplementary Fig. S30), consistent with previous findings on low cytotoxicity and excellent biocompatibility of the constituent materials $^{20,33,53-57}$.

Discussion

Chemical synthesis, materials engineering, and applications presented here describe a low-cost, scalable, monolithic 3D fabrication strategy for soft, stretchable, transient electronics. Physical/chemical combination of various organic materials enabled development of biodegradable/biocompatible insulating, semiconducting, and conducting materials that could be deposited by solution casting, without compromising the integrity of underlying layers, and patterned with micron-level precision using optical lithography. Sequential, layer-by-layer deposition of electronic materials under optimized conditions produced diverse functional components, including strain, temperature, pressure, and EP sensors, as well as organic transistors. As a proof-of-concept bioelectronic device, EP sensing electrode arrays demonstrated the ability to not only monitor neural and cardiac activities with high spatiotemporal resolution but also provide therapeutic functions for potential clinical interventions such as suppressing epileptic

seizures and capturing cardiac rhythms. The proposed facile and costeffective manufacturing strategies are expected to be further applicable to bio-integrated electronics and eco-friendly consumer electronics, paving the way for advancements in transient electronics.

Methods

Synthesis of UV-PLCL

L-lactide (LA, TCI, Japan; 60 mmol), ε-caprolactone (ε-CL, Sigma-Aldrich, USA; 60 mmol), 1,4-butanediol (Sigma-Aldrich, USA; 12, 24, and 48 mmol for PLCL prepolymers with molecular weights of 2 k, 1 k, and 0.5 k, respectively), and stannous octoate (Sn(Oct)2, Sigma-Aldrich, USA; 1.2 mmol) were added into a dried three-neck flask and magnetically stirred at 300 rpm to ensure homogeneous mixing. After purging three times with N₂ at 90 °C, the flask was sealed under vacuum and heated in an oil bath at 150 °C for 24 h, followed by cooling to room temperature (RT). Subsequently, the resulting PLCL prepolymers were reacted with isophorone diisocyanate (IPDI, Sigma-Aldrich, USA) and 2-hydroxyethyl acrylate (2-HEA, Sigma-Aldrich, USA) at a ratio of 1:2:2 in 1,4-butanediol:IPDI:2-HEA. IPDI, dissolved in dimethylformamide (DMF), was added dropwise to the flask and heated at 60 °C for 6 h before cooling to RT. Then, 2-HEA was added dropwise to the flask, heated at 45 °C for 3 h, and cooled to RT again. The resulting product was purified with CE tubing (Repligen, USA, MWCO: 0.1~0.5kD) to remove the catalyst and unreacted monomers and subsequently dried in a vacuum oven at 80 °C overnight. The final product, UV-PLCL, was characterized by ¹H nuclear magnetic resonance (1H-NMR), Fourier transform infrared (FT-IR), and differential scanning calorimetry (DSC).

Synthesis of double-branched diazirine as a UV-responsive cross-linker

Sebacoyl chloride (Sigma-Aldrich, USA; 2.20 mM) and 2.5 mL of dichloromethane (DCM, Sigma-Aldrich, USA) were introduced into a 50-mL round-bottom flask covered with aluminum foil, purged three times with N_2 , and cooled to 0 °C in an iced beaker, followed by stirring for 10 min. Subsequently, this stirring solution was slowly added dropwise with 2,4-diethyl-1,5-pentanediol (Sigma-Aldrich, USA; 1 mM) dissolved in 5 mL of DCM and gradually returned to RT. After the reaction for 10 h, 4-[3-(trifluoromethyl)-3H-diazirin-3-yl]benzyl alcohol (TCI, Japan; 0.475 mM) dissolved in 2.5 mL of DCM was added dropwise to the flask, and the reaction was allowed to continue overnight. Removal of the solvent under vacuum at RT yielded a light yellowish viscous liquid, referred to as the double-branched diazirine cross-linker. The chemical structure of the synthesized polymer was characterized by 1 H-NMR.

Formation of insulator/conductor/semiconductor patterns

Insulator. The synthesized UV-PLCL was blended with 5 wt% of 2,4,6-trimethylbenzoyldiphenylphosphine oxide (TPO, Sigma-Aldrich, USA) as a photoinitiator, 5 wt% of trimethylolpropane tris(3-mercaptopropionate) (Sigma-Aldrich, USA) as a crosslinking enhancer, and ethyl acetate (EA, Daejungchem, Korea) to achieve a 50% w/v concentration of solution. This solution was spin-cast onto a substrate at 3000 rpm for 30 s and baked on a hotplate at 70 °C for 5 min under sealed conditions. Subsequently, the film (thickness, ~ 2 μ m) was exposed to UV light at a wavelength of 365 nm (intensity: 18 mW/cm²) for 3 min through a mask using a mask aligner (MDA-400N, Midas System, Korea), followed by post-exposure bake (PEB) at 140 °C for 5 min to increase the degree of crosslinking in the exposed area. The film was then gently developed with EA to dissolve the unexposed area and baked at 100 °C for 5 min to remove residual solvent.

Conductor. Poly(3,4-ehylenedioxythiophene):poly(styrenesulfonate) (PEDOT:PSS, Clevios PH1000, Heraeus GmbH, Germany; solid content: 1.0-1.3 wt%) was blended with an appropriate amount of 2,4-

hexadiyne-1,6-diol (HDD, Sigma-Aldrich, USA) as a crosslinker, and 5 wt % of nonionic fluorosurfactant (Zonyl FS-300, ALFA Chemistry, USA) as a surfactant. This solution was spin-cast onto a substrate at 1,000 rpm for 30 s and baked on a hotplate at 100 °C for 90 s. Then, the film (thickness, -140 nm) was exposed to 254 nm UV light (intensity: 1.78 mW/cm²) at a distance of -5 cm for 5 min through a mask using a hand lamp (VL-215C, Vilber Lourmat, France), underwent PEB at 100 °C for 1 min, and developed in deionized (DI) water for 1 min. To improve electrical conductivity, the obtained conductor pattern was soaked in diluted (40% v/v in DI) sulfuric acid (H₂SO₄, SAMCHUN Chem., Korea) for 2 min and thoroughly rinsed with DI water, followed by baking at 100 °C for 1 min.

Semiconductor. A poly(3-hexylthiophene) (P3HT, Sigma-Aldrich, USA) solution at a concentration of 10 mg/mL in xylene (Sigma-Aldrich, USA) was heated to 60 °C to ensure homogeneous dissolution and then cooled to -20 °C for 1 h, promoting the self-assembly of P3HT monomers into nanofibers (NFs) through π - π stacking. Xylene was chosen among various organic solvents due to its appropriate P3HT solubility for the NF formation. The resulting P3HT-NF solution was mixed with a PLCL solution (10 mg/mL in xylene) at a weight ratio of 8:2 in PLCL:P3HT, supplemented with 5 wt% of Zonyl FS-300 as a surfactant and 5 wt% of pre-synthesized double-branched diazirine as a crosslinker. This solution was spin-cast on glass substrate at 2000 rpm for 30 s, followed by baking on a hotplate at 110 °C for 5 min. The resulting film (thickness, ~200 nm) was patterned through sequential steps of exposure to 365 nm UV light (intensity: 18 mW/cm²) for 3 min through a mask using a mask aligner, curing at 140 °C for 5 min, development with xylene, and final baking at 110 °C for 5 min.

Fabrication of functional electronic components

A stretchable, transient organic thin film transistor (OTFT) in an inverted coplanar structure (bottom gate bottom contact, BGBC) was fabricated through a layer-by-layer stacking of electronic materials following the photopatterning procedures described above. Initially, a sacrificial layer was created on a glass substrate by spin-coating a 20 wt % solution of poly(acrylic acid) (PAA, Sigma-Aldrich, USA; Mw, ~100k) in water at 3000 rpm for 30 s, followed by curing at 150 °C for 2 min. After depositing a layer of UV-PLCL (~20 µm) as a substrate, a thin conductor layer (~100 nm) was patterned to serve as a gate electrode. Another layer of UV-PLCL (~1 µm) was used as a gate dielectric. Then, source/drain electrodes, with channel length and width of 50 µm and 500 µm, respectively, were formed by patterning a layer of conductor (~100 nm), followed by deposition of a semiconducting layer (thickness ~1 µm) to create a channel. Finally, the fabricated OTFT was released from the glass substrate by dissolving the PAA sacrificial layer in DI water at 60 °C. Additionally, other electronic components, such as strain sensor, temperature sensor/heater, pressure sensor, and electrophysiology (EP) sensor, were fabricated on PAA/glass substrate using a similar sequential stacking process of electronic materials, following the device structures depicted in Fig. 3.

Fabrication of soft, conformal, transient neural/cardiac electrode arrays

Soft, conformal, transient neural/cardiac electrode arrays (25 channels; single channel area, 0.04 mm² for neural electrodes and 0.25 mm² for cardiac electrodes) were fabricated on a PAA/glass substrate through a sequential deposition/patterning process of an insulator layer as substrate, a conductor layer as recording/electrical stimulation electrodes, and another insulator layer as encapsulation. The arrays were then released from the substrate in DI water at 60 °C and connected with an ACF cable for external connection to a recording system. To assess the recording/electrical stimulation capabilities, electrochemical impedance spectroscopy (EIS) and cyclic voltammetry (CV) were conducted using a potentiostat (Compact-stat, Ivium

Technologies, Netherlands) in 1x PBS (pH 7) solution. A standard electrochemical cell setup with three electrodes, consisting of a platinum (Pt) wire electrode, an Ag/AgCl electrode, and the fabricated electrode arrays, as the counter, reference, and working electrodes, respectively, was utilized. EIS involved sinusoidal wave scanning (frequency, 1 Hz - 10 kHz; amplitude, 10 mV), while CV was performed with a scan rate of 20 mV/s within a voltage range of -0.6 V to 0.6 V.

In vivo neural recording and stimulation

Experiments were performed in Sprague-Dawley rats (Orient Bio Inc., Seongnam, Korea). The International Genetic Standardization (IGS) system ensures genetic stability and uniformity of the SD strain. Male rats, aged 12 weeks and weighing 450-520 g at the time of the experiment, were used. Animals were maintained in specific pathogen-free (SPF) conditions under a 12 h light/dark cycle, with controlled temperature and humidity, and with free access to food and water. All animal experiments were performed in accordance with the Korean Ministry of Food and Drug Safety Guide for the Care and Use of Laboratory Animals and were conducted according to protocols approved by the Institutional Animal Care and Use Committees (IACUC). This study was reviewed and approved by the IACUC of Samsung Biomedical Research Institute (SBRI) (Approval Numbers: SBRI-IACUC-20221209002). SBRI is an Association for Assessment and Accreditation of Laboratory Animal Care International (AAALAC International) accredited facility and abide by the Institute of Laboratory Animal Resources (ILAR) guide. The animals were anesthetized by inhaling isoflurane (concentrations ranging from 3 % to 5 %, O₂ level: 0.1 L min⁻¹), and remained under anesthesia throughout the device implantation. For implantation of the neural array, a craniotomy was performed to expose a 6 × 8 mm cortical region on either the left or right hemisphere. A soft, conformal, transient neural electrode array was then placed on the exposed cortical surface. Three commercial screw electrodes (19010-10, FST, USA) were inserted into the contralateral skull: two for control and one as a reference electrode. The implanted array enabled discrimination between normal EEG activity and penicillin-induced acute seizures. EEG signals were acquired using a multichannel amplifier (Nicolet v32 amplifier, Natus, USA) and a signal acquisition system (NicVue Connect HL7, Natus, USA, 500 samples per second). The focal acute seizure was induced by the injection of penicillin (500 IU) into the cortex (AP -3 mm, ML 3 mm). Seizure activity was elicited immediately, exhibiting distinct signal characteristics that enabled straightforward analysis. Signal quality was quantified by calculating the signal-to-noise ratio (SNR), defined as the ratio of the spike amplitude to background ECoG amplitude, and compared with that obtained using a device composed of Au.

Electrical stimulation (model 2100, AM systems, USA, biphasic, 130 Hz, 100 μA , 10 min) was applied to observe the inhibitory effect of drug-induced epileptic seizures. The analysis of epileptic spikes was conducted by applying a bandpass filter with a passband of 10-50 Hz to the measured signal. Three noise-free bins of one minute each were extracted from the data before and after the electrical stimuli were applied. Peaks exceeding 200 μV were automatically identified within each dataset. These peaks underwent both visual inspection and correction for any potential errors. Finally, for each dataset, the number of spikes was measured, and their amplitude was calculated to determine the mean and standard error of the mean.

To ensure long-term implantation and prevent interference from animal movements, the array and skull were encapsulated in dental cement and protected with a custom-made crown. Throughout the 8-week study period, animals were anesthetized once per week for ECoG recordings, and neural signals were collected for 10 minutes using the implanted array. The power spectral density for each signal was determined using the Welch method, which is considered a reliable and efficient approach for analyzing the dynamics of physiological signals.

Biocompatibility test

To confirm the biocompatibility of the materials and devices, a tenweek implantation study was conducted on rats using transient neural electrodes. Tissue samples were collected from the rats in the control group and from rats that had been implanted ten weeks prior. Subsequently, the investigation focused on biological responses, utilizing immunohistochemistry. The following primary antibodies were used in the immunohistochemistry procedure: TNF- α (Abcam, ab6671, 1:200) and CD68 (Abcam, ab125212, 1:200). The sections were then subjected to an overnight incubation with primary antibodies at 4 °C. This was followed by visualization using diaminobenzidine (DAB) and hematoxylin counterstaining.

Reporting summary

Further information on research design is available in the Nature Portfolio Reporting Summary linked to this article.

Data availability

All data supporting the findings and conclusions of this study are available within the paper and its Supplementary Information files. Source data are provided with this paper. All other relevant data are available from the corresponding author upon request. Source data are provided with this paper.

References

- Kang, S. K. et al. Bioresorbable silicon electronic sensors for the brain. Nature 530, 71-76 (2016).
- Boutry, C. M. et al. A stretchable and biodegradable strain and pressure sensor for orthopaedic application. *Nat. Electron.* 1, 314–321 (2018).
- Lee, J. et al. Flexible, sticky, and biodegradable wireless device for drug delivery to brain tumors. Nat. Commun. 10, 5205 (2019).
- Boutry, C. M. et al. Biodegradable and flexible arterial-pulse sensor for the wireless monitoring of blood flow. Nat. Biomed. Eng. 3, 47–57 (2019).
- Shin, J. et al. Bioresorbable pressure sensors protected with thermally grown silicon dioxide for the monitoring of chronic diseases and healing processes. *Nat. Biomed. Eng.* 3, 37–46 (2019).
- Choi, Y. S. et al. Fully implantable and bioresorbable cardiac pacemakers without leads or batteries. *Nat. Biotechnol.* 39, 1228–1238 (2021).
- Reeder, J. T. et al. Soft, bioresorbable coolers for reversible conduction block of peripheral nerves. Science 377, 109–115 (2022).
- Cho, M. et al. Fully bioresorbable hybrid opto-electronic neural implant system for simultaneous electrophysiological recording and optogenetic stimulation. *Nat. Commun.* 15, 2000 (2024).
- Bae, J. Y. et al. A biodegradable and self-deployable electronic tent electrode for brain cortex interfacing. *Nat. Electron.* 7, 815–828 (2024).
- Peng, X. et al. A breathable, biodegradable, antibacterial, and selfpowered electronic skin based on all-nanofiber triboelectric nanogenerators. Sci. Adv. 6, eaba9624 (2020).
- Baumgartner, M. et al. Resilient yet entirely degradable gelatinbased biogels for soft robots and electronics. *Nat. Mater.* 19, 1102–1109 (2020).
- Ko, G. J. et al. Biodegradable, flexible silicon nanomembrane-based NOx gas sensor system with record-high performance for transient environmental monitors and medical implants. NPG Asia Mater. 12, 71 (2020).
- Yoon, H. J. et al. Biodegradable, three-dimensional colorimetric fliers for environmental monitoring. Sci. Adv. 8, eade3201 (2022).
- Min, J. K. et al. Recent advances in biodegradable green electronic materials and sensor applications. Adv. Mater. 35, e2211273 (2023).

- Lopez Hernandez, H. et al. Triggered transience of metastable poly(phthalaldehyde) for transient electronics. Adv. Mater. 26, 7637–7642 (2014).
- 16. Park, C. W. et al. Thermally triggered degradation of transient electronic devices. *Adv. Mater.* **27**, 3783–3788 (2015).
- Shin, J. W. et al. Biologically safe, degradable self-destruction system for on-demand, programmable transient electronics. ACS Nano 15, 19310–19320 (2021).
- Han, W. B., Lee, J. H., Shin, J. W. & Hwang, S. W. Advanced materials and systems for biodegradable, transient electronics. *Adv. Mater.* 32, e2002211 (2020).
- Shim, J. S., Rogers, J. A. & Kang, S. K. Physically transient electronic materials and devices. *Mater. Sci. Eng. R. Rep.* 145, 100624 (2021).
- Jang, T. M. et al. Stretchable and biodegradable self-healing conductors for multifunctional electronics. Sci. Adv. 10, eadp9818 (2024).
- Kang, S. H. et al. Fully biodegradable electrochromic display for disposable patch. npj Flex. Electron. 8, 72 (2024).
- Mitra, K. Y., Willert, A., Chandru, R., Baumann, R. R. & Zichner, R. Inkjet Printing of Bioresorbable Materials for Manufacturing Transient Microelectronic Devices. Adv. Eng. Mater. 22, 2000547 (2020).
- 23. Pietsch, M. et al. Biodegradable inkjet-printed electrochromic display for sustainable short-lifecycle electronics. *J. Mater. Chem. C.* **8**, 16716–16724 (2020).
- 24. Heiden, A. et al. 3D printing of resilient biogels for omnidirectional and exteroceptive soft actuators. Sci. Robot. 7, eabk2119 (2022).
- Fumeaux, N. & Briand, D. 3D printing of customizable transient bioelectronics and sensors. Adv. Electron. Mater. 10, 2400058 (2024).
- Shou, W. et al. Low-cost manufacturing of bioresorbable conductors by evaporation-condensation-mediated laser printing and sintering of Zn nanoparticles. Adv. Mater. 29, 1700172 (2017).
- Feng, S., Cao, S., Tian, Z., Zhu, H. & Kong, D. Maskless patterning of biodegradable conductors by selective laser sintering of microparticle inks and its application in flexible transient electronics. ACS Appl. Mater. Interfaces 11, 45844–45852 (2019).
- 28. Yang, Q. et al. High-speed, scanned laser structuring of multilayered eco/bioresorbable materials for advanced electronic systems. *Nat. Commun.* **13**, 6518 (2022).
- Wang, C. et al. Monitoring of the central blood pressure waveform via a conformal ultrasonic device. *Nat. Biomed. Eng.* 2, 687–695 (2018).
- Wang, Z. et al. Conformal in-ear bioelectronics for visual and auditory brain-computer interfaces. *Nat. Commun.* 14, 4213 (2023).
- 31. Zhao, X. et al. A reconfigurable and conformal liquid sensor for ambulatory cardiac monitoring. *Nat. Commun.* **15**, 8492 (2024).
- 32. Jeong, S. I. et al. In vivo biocompatibility and degradation behavior of elastic poly(L-lactide-co-ε-caprolactone) scaffolds. *Biomaterials* **25**, 5939–5946 (2004).
- 33. Han, W. B. et al. Ultra-stretchable and biodegradable elastomers for soft, transient electronics. *Nat. Commun.* **14**, 2263 (2023).
- 34. Kim, S. K. & Guymon, C. A. Effects of polymerizable organoclays on oxygen inhibition of acrylate and thiol-acrylate photopolymerization. *Polymer* **53**, 1640–1650 (2012).
- 35. Chen, Q. et al. Exceptionally recyclable, extremely tough, vitrimer-like polydimethylsiloxane elastomers via rational network design. *Matter* **6**, 3378–3393 (2023).
- 36. Cooper, C. B. et al. Toughening stretchable fibers via serial fracturing of a metallic core. *Sci. Adv.* **5**, eaat4600 (2019).
- Han, W. B. et al. Zebra-inspired stretchable, biodegradable radiation modulator for all-day sustainable energy harvesters. Sci. Adv. 9, eadf5883 (2023).

- Shin, J. W. et al. Highly elastic, bioresorbable polymeric materials for stretchable, transient electronic systems. *Nano-Micro Lett.* 16, 102 (2024).
- 39. Shin, M. et al. Polythiophene nanofibril bundles surface-embedded in elastomer: A route to a highly stretchable active channel layer. *Adv. Mater.* **27**, 1255–1261 (2015).
- 40. Park, S., Lee, C. W. & Kim, J. M. Highly conductive PEDOT:PSS patterns based on photo-crosslinkable and water-soluble diacetylene diol additives. *Org. Electron.* **58**, 1–5 (2018).
- Zhao, H. et al. Biodegradable germanium electronics for integrated biosensing of physiological signals. Npj Flex. Electron. 6, 63 (2022).
- Lee, S.-M. et al. Ecofriendly transfer printing for biodegradable electronics using adhesion controllable self-assembled monolayers. Adv. Funct. Mater. 34, 2310612 (2024).
- Salvatore, G. A. et al. Biodegradable and highly deformable temperature sensors for the internet of things. Adv. Funct. Mater. 27, 1702390 (2017).
- 44. Basarir, F. et al. Edible and biodegradable wearable capacitive pressure sensors: A paradigm shift toward sustainable electronics with bio-based materials. *Adv. Funct. Mater.* **34**, 2403268 (2024).
- Hou, C. et al. A biodegradable and stretchable protein-based sensor as artificial electronic skin for human motion detection. Small 15, e1805084 (2019).
- Zheng, Y. et al. A molecular design approach towards elastic and multifunctional polymer electronics. Nat. Commun. 12, 5701 (2021).
- Li, Y. et al. Achieving tissue-level softness on stretchable electronics through a generalizable soft interlayer design. *Nat. Commun.* 14, 4488 (2023).
- Shim, H. et al. Elastic integrated electronics based on a stretchable n-type elastomer-semiconductor-elastomer stack. Nat. Electron. 6, 349–359 (2023).
- 49. Vo, N. T. P. et al. Autonomous self-healing supramolecular polymer transistors for skin electronics. *Nat. Commun.* **15**, 3433 (2024).
- Hu, Z. et al. Flexible Neural Interface From Non-Transient Silk Fibroin With Outstanding Conformality, Biocompatibility, and Bioelectric Conductivity. Adv. Mater. 36, e2410007 (2024).
- 51. Park, Y. G. et al. In-vivo integration of soft neural probes through high-resolution printing of liquid electronics on the cranium. *Nat. Commun.* **15**, 1772 (2024).
- 52. Boufidis, D., Garg, R., Angelopoulos, E., Cullen, D. K. & Vitale, F. Bioinspired electronics: Soft, biohybrid, and "living" neural interfaces. *Nat. Commun.* **16**, 1861 (2025).
- Lim, J. H. et al. Synthesis of shape-programmable elastomer for a bioresorbable, wireless nerve stimulator. *Biosens. Bioelectron.* 254, 116222 (2024).
- Klouda, L., Hacker, M. C., Kretlow, J. D. & Mikos, A. G. Cytocompatibility evaluation of amphiphilic, thermally responsive and chemically crosslinkable macromers for in situ forming hydrogels. *Biomaterials* 30, 4558–4566 (2009).
- 55. Lu, B. et al. Pure PEDOT:PSS hydrogels. *Nat. Commun.* **10**, 1043 (2019).
- Costamagna, F. et al. Nanotoxicology at the particle/micelle frontier: influence of core-polymerization on the intracellular distribution, cytotoxicity and genotoxicity of polydiacetylene micelles.
 Nanoscale 12, 2452–2463 (2020).
- 57. Chandel, A. K. S. et al. Injectable, shear-thinning, photocrosslinkable, and tissue-adhesive hydrogels composed of diazirine-modified hyaluronan and dendritic polyethyleneimine. *Biomater. Sci.* **12**, 1454–1464 (2024).

Acknowledgements

This work was supported by the national Research Foundation of Korea (NRF) grants funded by the Korea government (the Ministry of Science, ICT, MSIT) (RS- 2022- 00165524 and RS-2024-00459269).

Author contributions

W.B.H., S.H. and T.K. contributed equally to this work. W.B.H., S.H. and S.-W.H. designed the research and led the experiments. T.-M.J. and G.J.K. contributed to device fabrication and data analysis. W.B.H., S.H., T.K., J.J. and T.K. performed animal tests. W.B.H., S.H., T.K. and S.-W.H. wrote the manuscript with the advice of K.-S.L., Y.-M.S., E.P. and V.R.N. All authors read and approved the manuscript.

Competing interests

The authors declare no competing interests.

Additional information

Supplementary information The online version contains supplementary material available at https://doi.org/10.1038/s41467-025-64256-7.

Correspondence and requests for materials should be addressed to Suk-Won Hwang.

Peer review information *Nature Communications* thanks Dmitry Kireev, who co-reviewed with Pritom Chowdhury, and the other, anonymous, reviewer(s) for their contribution to the peer review of this work. A peer review file is available.

Reprints and permissions information is available at http://www.nature.com/reprints

Publisher's note Springer Nature remains neutral with regard to jurisdictional claims in published maps and institutional affiliations.

Open Access This article is licensed under a Creative Commons Attribution-NonCommercial-NoDerivatives 4.0 International License, which permits any non-commercial use, sharing, distribution and reproduction in any medium or format, as long as you give appropriate credit to the original author(s) and the source, provide a link to the Creative Commons licence, and indicate if you modified the licensed material. You do not have permission under this licence to share adapted material derived from this article or parts of it. The images or other third party material in this article are included in the article's Creative Commons licence, unless indicated otherwise in a credit line to the material. If material is not included in the article's Creative Commons licence and your intended use is not permitted by statutory regulation or exceeds the permitted use, you will need to obtain permission directly from the copyright holder. To view a copy of this licence, visit http://creativecommons.org/licenses/by-nc-nd/4.0/.

© The Author(s) 2025